Research Article Vol. 33, No. 2 / 27 Jan 2025 / Optics Express 2205

Optics EXPRESS

Integrated all-optical nonreciprocity based on a moving index grating

LEI TANG,[1,*] JIANG-SHAN TANG,[2] AND KEYU XIA[2,3,4]

[1] *College of Physics and Electronic Engineering, Institute of Solid State Physics, Sichuan Normal University, Chengdu 610101, China*
[2] *College of Engineering and Applied Sciences, National Laboratory of Solid State Microstructures, and Collaborative Innovation Center of Advanced Microstructures, Nanjing University, Nanjing 210023, China*
[3] *Shishan Laboratory, Suzhou Campus of Nanjing University, Suzhou 215000, China*
[4] *keyu.xia@nju.edu.cn*
[*] *tanglei@sicnu.edu.cn*

Abstract: Optical nonreciprocal devices are critical components in integrated photonic systems and scalable quantum technologies. We propose an all-optical approach to achieve integrated optical nonreciprocity utilizing a moving index grating. The grating is generated in a nonlinear optical waveguide through the Kerr effect by driving the waveguide with two counter-propagating pump fields of slightly different frequencies. Based on this moving index grating, our system exhibits exceptional versatility by achieving both nonreciprocal transmission and reflection of signal fields. We obtain an all-optical isolator that achieves near-unity isolation contrast and negligible insertion loss while effectively addressing the dynamic reciprocity challenge. Our protocol establishes a novel approach for achieving integrated all-optical nonreciprocal devices, paving the way for advanced integrated photonic circuits.

1. Introduction

Integrated nonreciprocal devices, such as optical isolators and circulators, are indispensable components in advanced photonic systems and quantum information technologies. These devices play crucial roles in preventing unwanted back-reflections in integrated photonic systems [1–3], enabling unidirectional signal propagation in optical communication networks [4,5], facilitating the manipulation and routing of quantum states in quantum communication and computing devices [6–8], and supporting the development of compact, efficient photonic sensors and metrology tools [9–12]. The magneto-optical effect has been traditionally employed to achieve optical isolation [13–16]. However, its reliance on bulky components, such as external magnets, renders it impractical for integrated photonic applications. Consequently, realizing integrated optical isolation remains one of the most significant challenges in the field of photonics. Various innovative approaches for realizing integrated optical isolation have been demonstrated, addressing the limitations of traditional magneto-optical methods, including optical nonlinear processes [11,17–29], spatiotemporal modulation of optical mediums [30–36], chiral light-matter interactions [37–42], directional optomechanical interactions [43–47]. Despite significant progress in the development of magnetic-free integrated nonreciprocal devices, achieving all-optical isolation with a simple and scalable structure on a solid-state platform remains a substantial challenge.

Novel methods based on Bragg gratings offer a promising pathway to overcome this challenge and realize all-optical nonreciprocity. A Bragg grating is a periodic modulation of the refractive index along the core of an optical fiber or waveguide. Permanent gratings are typically created by exposing the core to an intense optical interference pattern, which induces localized changes in the material's refractive index [48–50]. Bragg gratings can achieve broad-band and near-unity back reflection, making them crucial components in various important applications across multiple

#546389 https://doi.org/10.1364/OE.546389
Journal © 2025 Received 28 Oct 2024; revised 18 Dec 2024; accepted 30 Dec 2024; published 15 Jan 2025

related fields. These applications include optical communications [51], fiber optic sensors [51,52], lasers [53,54], and Optical signal processing [55]. The versatility and efficiency of Bragg gratings in manipulating light have made them indispensable in modern photonics and optical technologies. Interestingly, periodic Bragg structures can be utilized to achieve optical nonreciprocity. This phenomenon can be realized through various means, including waveguide Bragg gratings [56,57], moving atomic Bragg mirrors [58], moving photonic lattices [59,60], and $\mathcal{PT}$-synthetic Bragg structures [61]. However, these reported schemes often rely on complex gratings [56,61], specially designed structures [57], or atom trapping [58–60], which typically require intricate fabrication processes, making them difficult to implement in integrated photonic circuits.

In our paper, we propose an all-optical method to achieve optical nonreciprocity. Unlike permanent Bragg gratings, our nonreciprocal system utilizes a moving index grating (MIG). This grating is generated in a nonlinear optical waveguide through the Kerr effect, induced by two counter-propagating pump fields. When two counter-propagating pump fields with identical frequency and intensity interact, they stimulate a standing-wave pattern in the nonlinear waveguide. If the pump fields are sufficiently strong, this standing-wave envelope imposes a periodic modulation on the waveguide's refractive index, creating a nonlinear index grating. By detuning the two pump fields, we can excite a moving wave envelope, resulting in a MIG within the waveguide. The dynamic characteristics of our grating play a pivotal role in achieving optical nonreciprocity. To investigate optical nonreciprocity, we introduce two weak signal fields into the waveguide from opposing directions. The Doppler effect induces distinct frequency shifts in the backscattered fields of the two weak signal fields interacting with the MIG. The unidirectional nature of the MIG breaks time-reversal symmetry, resulting in nonreciprocal transmission and reflection of the signal fields. Leveraging this nonreciprocal transmission, we can realize an all-optical isolator. Compared with previous nonreciprocal structures based on spatio-temporal modulation schemes [30,32,34–36], our approach utilizes an all-optical method to modulate the refractive index of the medium. This optical modulation significantly simplifies the implementation process, making it more practical for integrated photonic circuits. In contrast to many nonlinear nonreciprocal systems that are limited by dynamic reciprocity [1,11,17,20,21,25], our approach achieves dynamic nonreciprocity, allowing forward and backward signals to coexist simultaneously in the nonlinear system. Additionally, compared to systems relying on moving Bragg gratings in atomic platforms [58–60], our method operates on a solid-state platform, eliminating the need for atom trapping and stringent external controls. This makes our system more robust, scalable, and better suited for integration. Our approach offers several advantages, including tunability, all-optical control and compatibility with integrated photonic platforms. These features make our approach a promising and practical candidate for achieving nonreciprocal light propagation in integrated photonic applications.

2. Theoretical model of MIG

Consider a nonlinear optical waveguide, as shown in Fig. 1(a). The waveguide can be constructed from silicon nitride, which exhibits a high Kerr nonlinearity but has a low gain coefficient for stimulated Brillouin scattering (SBS). Two continuous wave pump fields in y polarization are incident from opposite directions, resulting in an interference pattern within the waveguide, as illustrated in Fig. 1(a). The pattern remains stationary when the pump fields share the same frequency; however, it shifts in response to the frequency difference between these pump fields. Due to the Kerr nonlinearity of the optical waveguide, a variation in the refractive index accompanies this field distribution. Consequently, an optical index grating is induced by the pump fields, as illustrated in Fig. 1(b). Furthermore, the mismatch in frequencies between the two pump fields initiates motion in the grating. It is worth noting that SBS is negligible in our system, primarily due to the relatively high phonon damping characteristic of the silicon nitride waveguide.

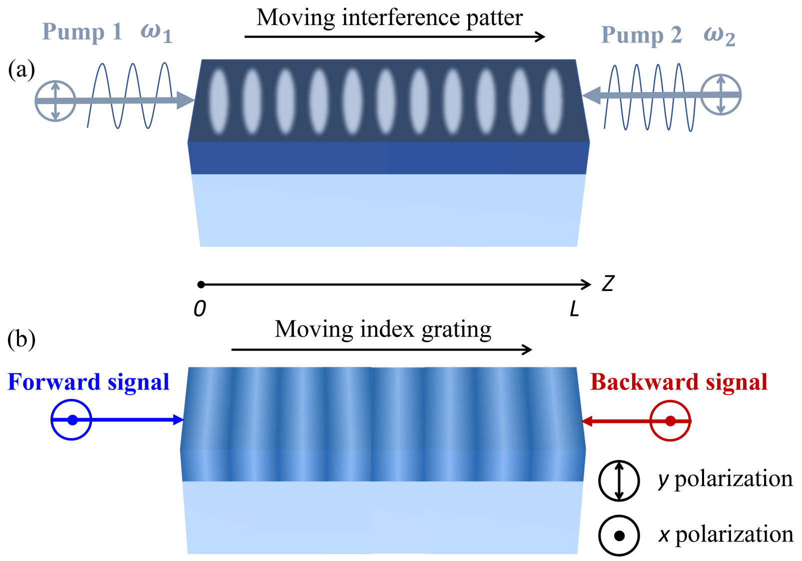

Fig. 1. Schematic diagram of the all-optical nonreciprocal system. (a) A moving interference pattern is generated in the optical waveguide by two continuous-wave pump fields (Pump 1 and Pump 2) with y-polarization and slightly different frequencies. (b) This interference pattern induces a moving index grating in the waveguide via the Kerr nonlinearity. The forward (backward) signal, with x-polarization, is incident from the left (right) side of the waveguide.

2.1. *Coupled amplitude equations*

The total pump field within the nonlinear waveguide comprises two counter-propagating pump fields (pump 1 and pump 2) along the z-axis. This field can be represented as $\tilde{E}_\mathrm{p} = A_1 e^{i(k_1 z - \omega_1 t)} + A_2 e^{i(-k_2 z - \omega_2 t)}$ + c.c., where we use the tilde to denote a quantity that varies rapidly in time. The amplitudes of pump 1 and pump 2 are denoted by A_1 and A_2, respectively. The wave vector magnitude is given by $k_i = n_0 \omega_i / c$ $(i = 1, 2)$, where n_0 represents the linear component of the refractive index, c is the the speed of light in vacuum, and ω_i is the frequency for each fields. Here we have ignored the dispersion in the waveguide since the frequency difference between the two pumps is small, on the order of a few gigahertz [62]. In a Kerr nonlinear material that responds instantaneously to the pump field, the modulated refractive index of the waveguide is expressed as $n = n_0 + n_\mathrm{NL}$. Here, $n_\mathrm{NL} = \bar{n}_2 \left\langle \tilde{E}_\mathrm{p}^2 \right\rangle$ represents the nonlinear contribution to the refractive index, where $\bar{n}_2 = n_0 n_2 \epsilon_0 c$ and $\left\langle \tilde{E}_\mathrm{p}^2 \right\rangle$ denotes the time average of $\tilde{E}_\mathrm{p}^2$. While n_2 refers to the second-order refractive index and ϵ_0 is the vacuum permittivity. Next, we can express the refractive index variation as

$$n_\mathrm{NL} = 2\bar{n}_2 \left\{ A_\mathrm{s} + \left[A_\mathrm{m} e^{i(qz - \Omega t)} + \mathrm{c.c.} \right] \right\} , \tag{1}$$

where we have introduced $q = k_1 + k_2$ and $\Omega = \omega_1 - \omega_2$ to represent the wave vector magnitude and the frequency of the index grating, respectively. The first term of Eq. (1) is for the stationary refractive index variation with $A_\mathrm{s} = A_1^2 + A_2^2$. The other terms are for the time-varying refractive index distribution with $A_\mathrm{m} = A_1 A_2$. When the pump fields meet the conditions $A_1 = A_2$ and $\Omega = 0$, the total pump field forms a standing wave, leading to a static grating in the waveguide.

Conversely, when $\Omega>0$ or $\Omega<0$, the index grating moves in the $\pm z$ direction at a velocity of $v = |\Omega/q|$.

To study optical nonreciprocity, two weak, x-polarized signal fields, $\tilde{E}^{+}_{\text{in}}$ and $\tilde{E}^{-}_{\text{in}}$, are incident from the forward and backward directions, respectively. Each field is scattered by the index grating and the backscattering field is denoted by $\tilde{E}^{\pm}_{\text{bs}}$. So, we have the total signal field $\tilde{E}^{\pm} = \tilde{E}^{\pm}_{\text{in}} + \tilde{E}^{\pm}_{\text{bs}}$ for the forward or backward incident case. The signal fields satisfy the wave equation $\nabla^2\tilde{E}^{\pm} - \frac{1}{\epsilon_0 c^2}\frac{\partial^2\tilde{D}^{\pm}}{\partial t^2} = 0$, where $\tilde{D}^{\pm} = \epsilon_0\epsilon_r\tilde{E}^{\pm}$ and $\epsilon_r = n^2$. Then, we can obtain $\frac{\partial^2\tilde{D}^{\pm}}{\partial t^2} = \epsilon_0[2(\frac{\partial n}{\partial t})^2\tilde{E}^{\pm} + 2n\frac{\partial^2 n}{\partial t^2}\tilde{E}^{\pm} + 4n\frac{\partial n}{\partial t}\frac{\partial\tilde{E}^{\pm}}{\partial t} + n^2\frac{\partial^2\tilde{E}^{\pm}}{\partial t^2}]$. Under the condition $|\Omega| \ll \omega_{1,2}$, the wave equation can be approximated as $\nabla^2\tilde{E}^{\pm} - \frac{n^2}{c^2}\frac{\partial^2\tilde{E}^{\pm}}{\partial t^2} = 0$. For the nonlinear waveguide, given that $n_{\text{NL}} \ll n_0$, the square of the total refractive index can be approximated as $n^2 = n_0^2 + 2n_0 n_{\text{NL}}$. Therefore, we can rewrite the wave equation as

$$\nabla^2\tilde{E}^{\pm} - \frac{n_0^2 + 2n_0 n_{\text{NL}}}{c^2}\frac{\partial^2\tilde{E}^{\pm}}{\partial t^2} = 0\,. \tag{2}$$

First, we investigate the transmission of the forward signal field. The total signal field in the waveguide is written as $\tilde{E}^{+} = E^{+}_{\text{in}}e^{i(kz-\omega t)} + E^{+}_{\text{bs}}e^{i(-k^{+}_{\text{bs}}z-\omega^{+}_{\text{bs}}t)} + \text{c.c.}$, where E^{+}_{in} and E^{+}_{bs} are the amplitudes, ω and ω^{+}_{bs} are the frequencies, k and k^{+}_{bs} are the wave vectors, of the incident field and its backscattering field, respectively. The backscattering field, generated by a MIG ($\Omega \neq 0$), exhibits a non-negligible Doppler effect. Consequently, the frequency of the backscattering field shifts to $\omega^{+}_{\text{bs}} = \omega - \Omega$. Subsequently, we substitute $\tilde{E}^{+}$ into Eq. (2) and analyze its component exhibiting spatial and temporal dependence, expressed as $\exp[i(kz-\omega t)]$. This part of Eq. (2) is expressed as

$$\frac{\partial^2 E^{+}_{\text{in}}}{\partial z^2} + 2ik_{+}\frac{\partial E^{+}_{\text{in}}}{\partial z} = -4A_{\text{s}}\frac{n_0\bar{n}_2\omega^2}{c^2}E^{+}_{\text{in}} - 4A_{\text{m}}\frac{n_0\bar{n}_2\omega^{+2}_{\text{b}}}{c^2}E^{+}_{\text{bs}}e^{-i\Delta q_{+}z}\,, \tag{3}$$

where we have defined the wave vector mismatch $\Delta q_{+} \equiv k + k^{+}_{\text{bs}} - q$ with $k^{+}_{\text{bs}} = n_0\omega^{+}_{\text{bs}}/c$. We then apply the slowly varying amplitude approximation, neglecting second-order derivatives. Using the relation $k = n_0\omega/c$, we rewrite Eq. (3) as

$$\frac{\partial E^{+}_{\text{in}}}{\partial z} = 2i\frac{\bar{n}_2\omega}{c}(A_{\text{s}}E^{+}_{\text{in}} + A_{\text{m}}E^{+}_{\text{bs}}e^{-i\Delta q_{+}z})\,. \tag{4}$$

A valid approximation has been made by replacing ω^{+}_{bs} with ω, given that $\Omega \ll \omega$. We next consider the portion of Eq. (2) that shows a spatial and temporal dependence given by $\exp[i(-k^{+}_{\text{bs}}z - \omega^{+}_{\text{bs}}t)]$. By applying the slowly varying amplitude approximation, we can obtain

$$\frac{\partial E^{+}_{\text{bs}}}{\partial z} = -2i\frac{\bar{n}_2\omega}{c}(A_{\text{s}}E^{+}_{\text{bs}} + A_{\text{m}}E^{+}_{\text{in}}e^{i\Delta q_{+}z})\,. \tag{5}$$

Second, we study the transmission of the backward-incident signal field. The total signal field is written as $\tilde{E}^{-} = E^{-}_{\text{in}}e^{i(-kz-\omega t)} + E^{-}_{\text{bs}}e^{i(k^{-}_{\text{bs}}z-\omega^{-}_{\text{bs}}t)} + \text{c.c.}$. Due to the Doppler effect of the MIG, the frequency of the backscattering field is shifted to $\omega^{-}_{\text{bs}} = \omega + \Omega$. Employing a similar approach, we can obtain the coupled amplitude equations

$$\frac{\partial E^{-}_{\text{in}}}{\partial z} = -2i\frac{\bar{n}_2\omega}{c}(A_{\text{s}}E^{-}_{\text{in}} + A_{\text{m}}E^{-}_{\text{bs}}e^{i\Delta q_{-}z})\,, \tag{6a}$$

$$\frac{\partial E^{-}_{\text{bs}}}{\partial z} = 2i\frac{\bar{n}_2\omega}{c}(A_{\text{s}}E^{-}_{\text{bs}} + A_{\text{m}}E^{-}_{\text{in}}e^{-i\Delta q_{-}z})\,, \tag{6b}$$

where we have defined the wave vector mismatch $\Delta q_{-} \equiv k + k^{-}_{\text{bs}} - q$ with $k^{-}_{\text{bs}} = n_0\omega^{-}_{\text{bs}}/c$. It is important to point out that our model do not account for any loss or absorption within the optical waveguide.

2.2. Solutions

To solve the coupled equations (Eqs. (4), (5), (6a) and (6b)), we set solutions form as

$$E_{\rm in}^{\pm}(z) = C_1^{\pm} e^{i\xi_1^{\pm} z} + C_2^{\pm} e^{i\xi_2^{\pm} z} \,, \tag{7a}$$

$$E_{\rm bs}^{\pm}(z) = \frac{\pm C_1^{\pm}\xi_1^{\pm} - 2\bar{n}_2 A_{\rm s} C_1^{\pm}\omega/c}{2\bar{n}_2 A_{\rm m}\omega/c} e^{i(\xi_1^{\pm} \pm \Delta q_{\pm})z} + \frac{\pm C_2^{\pm}\xi_2^{\pm} - 2\bar{n}_2 A_{\rm s} C_2^{\pm}\omega/c}{2\bar{n}_2 A_{\rm m}\omega/c} e^{i(\xi_2^{\pm} \pm \Delta q_{\pm})z} \,, \tag{7b}$$

where $\xi_1^{\pm} = (\mp\Delta q_{\pm} + \sqrt{\beta_{\pm}})/2$, $\xi_2^{\pm} = (\mp\Delta q_{\pm} - \sqrt{\beta_{\pm}})/2$, and $\beta_{\pm} = \Delta q_{\pm}^2 + 8\bar{n}A_{\rm s}\Delta q_{\pm}\omega/c + 16\bar{n}^2(A_{\rm s}^2 - A_{\rm m}^2)\omega^2/c^2$. To examine the system's nonreciprocal transmission, we assume equal amplitudes for the forward- and backward-incident signal fields. Under these boundary conditions, i.e., $E_{\rm in}^{+}(z=0) = E_{\rm in}^{-}(z=L) = E_0$ and $E_{\rm bs}^{+}(z=L) = E_{\rm bs}^{-}(z=0) = 0$, we can derive

$$C_1^{+} = \frac{E_0(\xi_2^{+} - 2\bar{n}_2 A_{\rm s}\omega/c)e^{i\xi_2^{+}L}}{(\xi_2^{+} - 2\bar{n}_2 A_{\rm s}\omega/c)e^{i\xi_2^{+}L} - (\xi_1^{+} - 2\bar{n}_2 A_{\rm s}\omega/c)e^{i\xi_1^{+}L}} \,, \tag{8a}$$

$$C_2^{+} = E_0 - C_1^{+} \,, \tag{8b}$$

$$C_1^{-} = \frac{E_0(\xi_2^{-} + 2\bar{n}_2 A_{\rm s}\omega/c)}{(\xi_2^{-} + 2\bar{n}_2 A_{\rm s}\omega/c)e^{i\xi_1^{-}L} - (\xi_1^{-} + 2\bar{n}_2 A_{\rm s}\omega/c)e^{i\xi_2^{-}L}} \,, \tag{8c}$$

$$C_2^{-} = -\frac{\xi_1^{-} + 2\bar{n}_2 A_{\rm s}\omega/c}{\xi_2^{-} + 2\bar{n}_2 A_{\rm s}\omega/c} C_1^{-} \,. \tag{8d}$$

The transmission (T_+) and reflection (R_+) of the forward signal field are defined as

$$T_{+} = \left|\frac{E_{\rm in}^{+}(z=L)}{E_{\rm in}^{+}(z=0)}\right|^2 \,, \quad R_{+} = \left|\frac{E_{\rm bs}^{+}(z=0)}{E_{\rm in}^{+}(z=0)}\right|^2 \,. \tag{9}$$

Similarly, the transmission (T_-) and reflection (R_-) of the backward signal field are defined as

$$T_{-} = \left|\frac{E_{\rm in}^{-}(z=0)}{E_{\rm in}^{-}(z=L)}\right|^2 \,, \quad R_{-} = \left|\frac{E_{\rm bs}^{-}(z=L)}{E_{\rm in}^{-}(z=L)}\right|^2 \,. \tag{10}$$

3. Nonreciprocal transmission and reflection

The solutions to the coupled equations enable the calculation of transmission and reflection from the MIG. The grating, induced by two pump fields with the equal amplitudes $A = 3 \times 10^7$ V/m and a frequency difference of $\Omega/2\pi = 3$ GHz, propagates at a velocity of 1.16×10^3 m/s. In Figs. 2(a) and 2(b), the transmission and reflection T_+ and R_+ (T_- and R_-) for the forward (backward) signal are plotted as functions of the incident signal frequency ω. As shown in Figs. 2(a) and 2(b), the MIG induces near-unity Bragg reflection (and near-zero transmission) for the forward and backward signal spectra. Specifically, the central frequency of the forward signal spectrum is located at $\omega_+/2\pi \approx 193.4096$ THz, while the central frequency of the backward signal spectrum is located at $\omega_-/2\pi \approx 193.4066$ THz. This results in a significant spectral shift of $\Delta = \omega_+ - \omega_- = 2\pi \times 3$ GHz between the forward and backward signals. Physically, the forward and backward signal fields experience opposite Doppler shifts induced by the directional MIG, given by $\omega_{\rm bs}^{\pm} = \omega \mp \Omega$, where Ω is the frequency difference between the pump fields. For the backward signal, the MIG satisfies the phase-matching condition near the central frequency $\omega_-/2\pi \approx 193.4066$ THz, resulting in strong Bragg reflection that blocks the backward transmission within a specific spectral window. Conversely, for the forward signal, the MIG causes a phase mismatch at ω_-, preventing Bragg reflection and allowing the forward signal to transmit through this frequency window. As a result, the forward signal propagates with

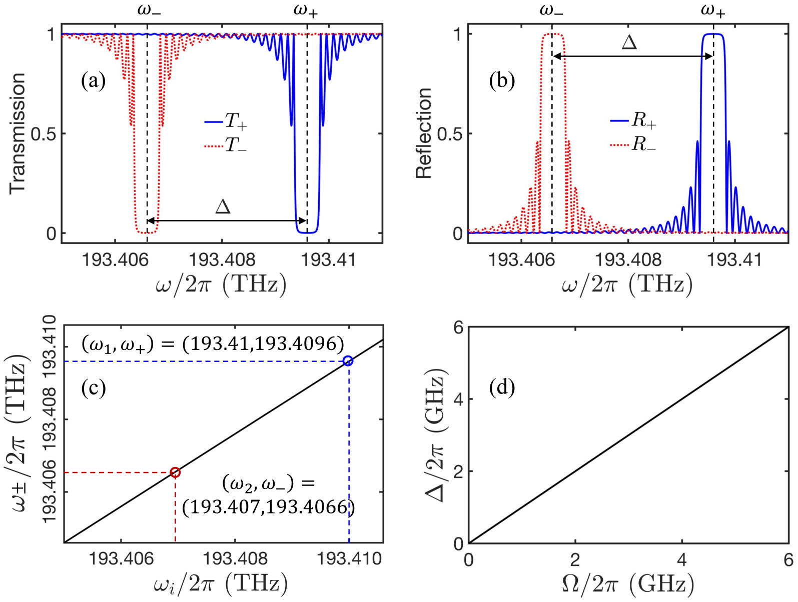

Fig. 2. (a) Transmission spectra for the forward (blue solid line) and backward (red dotted line) signal fields as functions of the signal frequency. The black dashed lines mark the minimum transmission points, corresponding to the central frequencies ω_+ and ω_- for the forward and backward signals, respectively. (b) Reflection spectra for the forward (blue solid line) and backward (red dotted line) signal fields as functions of the signal frequency. The black dashed lines indicate the maximum reflection points, corresponding to the central frequencies ω_+ and ω_- for the forward and backward signals, respectively. The pump frequencies in (a) and (b) are $\omega_1/2\pi = 193.410$ THz and $\omega_2/2\pi = 193.407$ THz, resulting in a frequency difference of $\Omega/2\pi = 3$ GHz. (c) The central frequencies of the forward (ω_+) and backward (ω_-) spectra as functions of the pump frequencies ω_1 and ω_2, respectively. (d) The spectrum shift Δ versus the pump frequency difference Ω. Other parameters are $L = 0.5$ m, $n_0 = 2$, $n_2 = 2.2 \times 10^{-19}$ m^2/W, and $A_1 = A_2 = A = 3 \times 10^7$ V/m.

negligible loss, while the backward signal is strongly reflected. This selective interaction with the MIG leads to a significant spectral shift $\Delta = \Omega$ between the forward and backward signals and enables nonreciprocal transmission and reflection in the nonlinear waveguide.

Furthermore, the position of the spectra can be precisely controlled by adjusting the pump frequencies. As shown in Fig. 2(c), the central frequencies ω_+ and ω_- shift linearly with the pump frequencies ω_1 and ω_2, respectively. For instance, increasing ω_2 results in a blueshift of the backward transmission spectrum. The blue and red circles indicate the central frequencies corresponding to specific pump frequencies: $(\omega_1, \omega_+) = (193.410, 193.4096)$ THz and $(\omega_2, \omega_-) = (193.407, 193.4066)$ THz, which are consistent with the results shown in Figs. 2(a) and 2(b). Consequently, the spectral shift Δ between the forward and backward spectra is directly determined by the frequency difference between the pump fields, i.e., $\Delta = \Omega$, as illustrated in Fig. 2(d). To achieve effective nonreciprocity, we need a sufficiently large frequency shift so that the forward and backward transmission spectra do not overlap. This separation creates a clear nonreciprocal spectral window. Moreover, a larger Ω helps minimize the insertion loss of the forward transmission in the nonreciprocal window. Therefore, by adjusting the pump frequencies, it is possible to fine-tune the position of the nonreciprocal window while optimizing overall device performance, including insertion loss and nonreciprocal bandwidth.

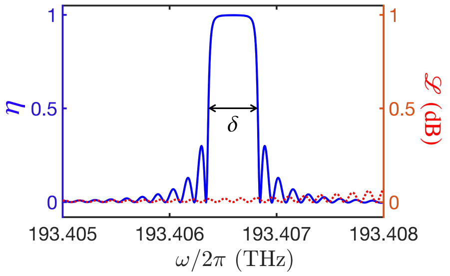

Fig. 3. Isolation contrast (blue solid line) and insertion loss (red dotted line) versus the signal frequency, the parameters are same as in Fig. 2(a).

As shown in Fig. 2(a), when the forward and backward transmission spectra are sufficiently separated by $\Delta/2\pi = 3\,\mathrm{GHz}$, the forward transmission reaches $T_+ \approx 1$, while the backward transmission drops to $T_- \approx 0$ at $\omega_-/2\pi \approx 193.4066\,\mathrm{THz}$. This corresponds to an isolation contrast of $\eta = (T_+ - T_-)/(T_+ + T_-) \approx 1$ and an insertion loss of $\mathscr{L} = -10\log(T_+) \approx 0$. Obviously, optical isolation for $T_+ \gg T_-$ is achieved with near-unity isolation contrast and negligible insertion loss. Figure 3 shows the isolation contrast η and the insertion loss $\mathscr{L}$ versus the signal frequency ω. It can be found that the maximal isolation contrast is achieved at the center of the backward transmission spectrum ($\omega_-/2\pi \approx 193.4066\,\mathrm{THz}$), where the backward transmission reaches its minimum value. The Full Width at Half Maximum (FWHM) of the

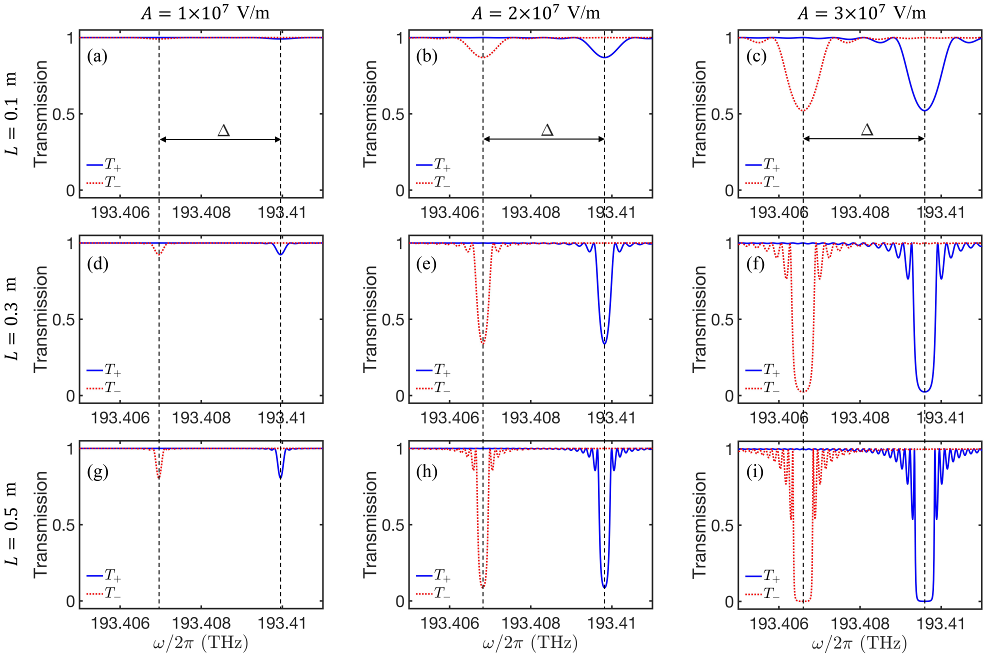

Fig. 4. Transmission spectra for the forward (blue solid lines) and backward (red dotted lines) signal fields as functions of the signal frequency for various pump amplitudes A and waveguide lengths L. The black dashed lines mark the minimum transmission points. The pump frequencies are $\omega_1/2\pi = 193.410\,\mathrm{THz}$ and $\omega_2/2\pi = 193.407\,\mathrm{THz}$, corresponding to a frequency difference of $\Omega/2\pi = 3\,\mathrm{GHz}$. Other parameters are $n_0 = 2$ and $n_2 = 2.2 \times 10^{-19}\,\mathrm{m}^2/\mathrm{W}$.

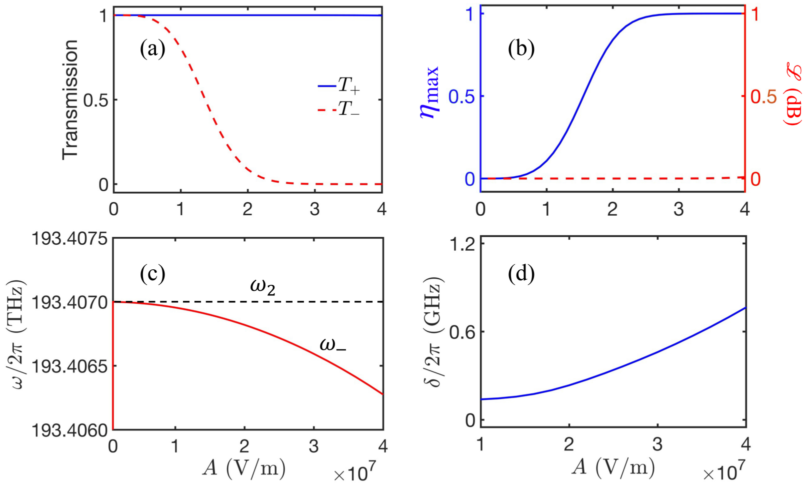

Fig. 5. (a) The minimal backward transmission T_- (red dashed line) and the corresponding forward transmission T_+ (blue solid line) versus the pump amplitude A. (b) The maximal isolation contrast $\eta_{\max}$ (blue solid line) and the corresponding insertion loss $\mathscr{L}$ (red dashed line) versus the pump amplitude A. (c) The signal frequency of the minimal backward transmission ω_- versus the pump amplitude A. The black dashed line is for the frequency of the backward pump field ω_2. (d) The FWHM of the isolation contrast δ versus the pump amplitude A. The parameters are $L = 0.5$ m, $n_0 = 2$, and $n_2 = 2.2 \times 10^{-19}$ m^2/W.

isolation contrast is $\delta \approx 0.46$ GHz, defining a frequency window for nonreciprocal transmission, as illustrated in Fig. 3. Within this nonreciprocal window, the insertion loss is negligible, as shown in Fig. 3.

The transmission spectra are influenced by both the pump amplitude A and the waveguide length L. For fixed pump frequencies, varying A and L changes the shape of the transmission spectra but does not affect the spectral shift Δ, as shown in Fig. 4. By increasing the pump amplitude A, the strength of the Bragg reflection increases, leading to a reduction in the minimum transmission and an expansion of the strong Bragg reflection window, as shown in Figs. 4(g), 4(h) and 4(i). Additionally, increasing the waveguide length also minimizes the minimum transmission, as shown in Figs. 4(b), 4(e) and 4(h). It is important to note that the central frequencies of the transmission spectra shift with increasing pump amplitude A due to the stationary refractive index variation, expressed as $n_{\rm NL}^{\rm s} = 2\bar{n}_2 A_{\rm s}$, which increases with A. This frequency shift is evident in Figs. 4(g), 4(h), and 4(i). However, the central frequencies remain unchanged when varying the waveguide length L, as $n_{\rm NL}^{\rm s}$ is independent of L, as shown in Figs. 4(c), 4(f) and 4(i). Since the transmission spectra are affected by A and L, these parameters can be adjusted to optimize the performance of the nonreciprocal transmission system.

We first investigate the influence of the pump amplitude A on the system's nonreciprocal transmission. As shown in Fig. 5(a), the minimum backward transmission decreases with increasing A, eventually approaching near zero. This phenomenon occurs because a higher pump field intensity induces a larger refractive index variation, which enhances the strength of the grating's reflection. By setting the pump frequency difference to $\Omega/2\pi = 3$ GHz, the MIG effectively prevents the overlap between the forward and backward spectra. Consequently, at the frequency corresponding to minimal backward transmission, the forward transmission remains nearly unity as the pump amplitude A increases within the range $0 \leqslant A \leqslant 4 \times 10^7$ V/m. As a result, the maximal isolation contrast $\eta_{\max}$ increases with A, reaching $\eta_{\max}$>0.99 when $A \geqslant 2.7 \times 10^7$ V/m. Once A exceeds approximately 3×10^7 V/m, further increases have little

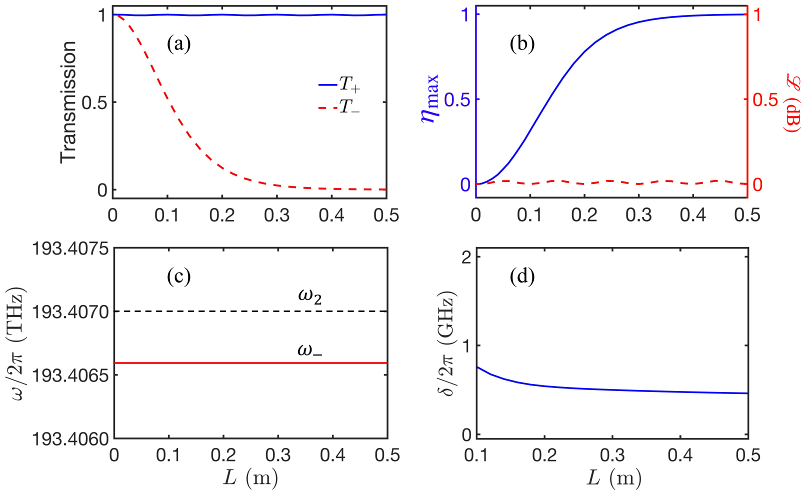

Fig. 6. (a) The minimal backward transmission T_- (red dashed line) and the corresponding forward transmission T_+ (blue solid line) versus the waveguide length L. (b) The maximal isolation contrast $\eta_{\max}$ (blue solid line) and the corresponding insertion loss $\mathscr{L}$ (red dashed line) versus the waveguide length L. (c) The signal frequency of the minimal backward transmission ω_- versus the waveguide length L. The black dashed line is for the frequency of the backward pump field ω_2. (d) The FWHM of the isolation contrast δ versus the waveguide length L. The parameters are $n_0 = 2$, $n_2 = 2.2 \times 10^{-19}$ m^2/W, and $A = 3 \times 10^7$ V/m.

effect on improving the isolation contrast. Additionally, the insertion loss remains negligible for $0<A \leqslant 4 \times 10^7$ V/m, as shown in Fig. 5(b). Due to the spectral shift induced by the stationary refractive index variation $n_{\mathrm{NL}}^{\mathrm{s}}$, the signal frequency of the minimum backward transmission (ω_-) gradually deviates from the backward pump frequency ω_2 as A increases, as illustrated in Fig. 5(c). Furthermore, the bandwidth of the nonreciprocal window δ increases with A, as shown in Fig. 5(d).

Next, we examine how the waveguide length L affects the nonreciprocal transmission properties of the system. As shown in Fig. 6(a), the minimal backward transmission, obtained at $\omega/2\pi =$ 193.4066 THz, decreases as the waveguide length L increases. In contrast, the forward transmission at the same frequency remains approximately equal to unity as the waveguide length L increases within the range of $0<L \leqslant 0.5$ m. Hence, the maximal isolation contrast $\eta_{\max}$ increases with L and reaches $\eta>0.99$ when $L \geqslant 0.4$ m, as shown in Fig. 6(b). The frequency of minimal backward transmission is $\omega_-/2\pi = 193.4066$ THz and remains unchanged with varying L, as illustrated in Fig. 6(c). This frequency deviates from the pump frequency ω_2 due to the stationary index variation $n_{\mathrm{NL}}^{\mathrm{s}}$, which is independent of the waveguide length L. Furthermore, the bandwidth of the nonreciprocal window δ exhibits a slight decrease as L increases, as shown in Fig. 6(d).

4. Discussion and conclusion

Our proposed nonreciprocal device offers significant practical advantages for experimental implementation. Silicon-nitride-based optical waveguides provide an excellent platform for our proposal, owing to their high Kerr nonlinearity, low propagation loss, and low gain coefficient for SBS [28,63,64]. Our method for achieving optical nonreciprocity utilizes a MIG, offering an all-optical approach. The MIG is generated by two intense, counter-propagating pump beams with a slight frequency detuning, which can be achieved using a tunable laser or an electro-optic modulator. These devices introduce a small frequency offset Ω between the two counter-propagating pump fields, which are launched into the same waveguide mode. To achieve optical nonreciprocity with an isolation contrast $\eta \approx 1$, the required pump laser intensity is approximately $I_{\mathrm{p}} = 2n\epsilon_0 cA^2 \approx 9.6\,W/\mu m^2$, assuming a pump amplitude $A = 3 \times 10^7$ V/m and a refractive index $n \approx 2$ [64,65], as shown in Fig. 3. Extending the waveguide length can effectively enhance the isolation contrast, allowing high isolation contrast to be achieved even with lower pump intensities. Furthermore, to observe the nonreciprocal transport, it is essential to remove the pump fields. However, due to the close proximity of the signal and pump frequencies, using a low-bandwidth filter to separate them poses significant practical challenges. Instead, as illustrated in Fig. 1, orthogonal polarization can be utilized to distinguish the signal and pump fields. Specifically, the pump fields are set to y-polarization, while the signal fields are set to x-polarization. Polarization beam splitters placed at both ends of the waveguide can then effectively separate and remove the pump fields, ensuring clean signal transmission. Regarding integrated implementation, the requirement for a relatively long optical waveguide poses a challenge for chip-level integration. However, photonic chips containing silicon nitride waveguides with physical lengths exceeding $L>1$ m have been successfully demonstrated experimentally [66]. By incorporating advanced design strategies, such as bent or coiled waveguides [66], the device footprint can be significantly reduced, enabling its implementation in integrated photonic circuits. While our work specifically focuses on strong index modulation induced by propagating pump waves via Kerr nonlinearity, our findings have broader implications. The principles we've uncovered can be generalized to other schemes, including acousto-optic [67–70] or nonlinear-gain [71] approaches.

In conclusion, we propose an integrated optical nonreciprocal system utilizing an all-optical method. Our system demonstrates the nonreciprocal transmission for weak signal fields, enabling the realization of an optical isolator with near-unity isolation contrast and negligible insertion loss. Meanwhile, our system can achieve nonreciprocal reflection, which expands its potential applications. Furthermore, our system addresses the dynamic reciprocity issue by utilizing a MIG generated by external pump fields. This innovative approach paves the way for all-optical, compact, and solid-state nonreciprocal devices in integrated photonic circuits.

Funding. National Natural Science Foundation of China (12305023, 12305020, 92365107); Sichuan Science and Technology Program (2024NSFSC1353); National Key Research and Development Program of China (2019YFA0308700); Program for Innovative Talents and Entrepreneurs in Jiangsu (JSSCTD202138); China Postdoctoral Science Foundation (2023M731613); Jiangsu Funding Program for Excellent Postdoctoral Talent (2023ZB708).

Disclosures. The authors declare no conflicts of interest.

Data availability. Data underlying the results presented in this paper are not publicly available at this time but may be obtained from the authors upon reasonable request.

References

1. D. Jalas, A. Petrov, M. Eich, *et al.*, "What is – and what is not – an optical isolator," Nat. Photonics **7**(8), 579–582 (2013).
2. J. Wang, S. Paesani, Y. Ding, *et al.*, "Multidimensional quantum entanglement with large-scale integrated optics," Science **360**(6386), 285–291 (2018).
3. J. Wang, F. Sciarrino, A. Laing, *et al.*, "Integrated photonic quantum technologies," Nat. Photonics **14**(5), 273–284 (2020).
4. T. Herr, V. Brasch, J. D. Jost, *et al.*, "Temporal solitons in optical microresonators," Nat. Photonics **8**(2), 145–152 (2014).
5. P. Ghelfi, F. Laghezza, F. Scotti, *et al.*, "A fully photonics-based coherent radar system," Nature **507**(7492), 341–345 (2014).
6. S. Wang, Z.-Q. Yin, W. Chen, *et al.*, "Experimental demonstration of a quantum key distribution without signal disturbance monitoring," Nat.Photonics **9**(12), 832–836 (2015).
7. A. Wallucks, I. Marinković, B. Hensen, *et al.*, "A quantum memory at telecom wavelengths," Nat. Phys. **16**(7), 772–777 (2020).
8. S. Daiss, S. Langenfeld, S. Welte, *et al.*, "A quantum-logic gate between distant quantum-network modules," Science **371**(6529), 614–617 (2021).
9. A. Lupaşcu, S. Saito, T. Picot, *et al.*, "Quantum non-demolition measurement of a superconducting two-level system," Nat. Phys. **3**(2), 119–123 (2007).
10. Y.-H. Lai, M.-G. Suh, Y.-K. Lu, *et al.*, "Earth rotation measured by a chip-scale ring laser gyroscope," Nat. Photonics **14**(6), 345–349 (2020).

11. K. Y. Yang, J. Skarda, M. Cotrufo, *et al.*, "Inverse-designed non-reciprocal pulse router for chip-based LiDAR," Nat. Photonics **14**(6), 369–374 (2020).
12. S. Welte, P. Thomas, L. Hartung, *et al.*, "A nondestructive bell-state measurement on two distant atomic qubits," Nat. Photonics **15**(7), 504–509 (2021).
13. H. Iwamura, S. Hayashi, and H. Iwasaki, "A compact optical isolator using a $Y_3Fe_5O_{12}$ crystal for near infra-red radiation," Opt. Quantum Electron. **10**(5), 393–398 (1978).
14. D. J. Gauthier, P. Narum, and R. W. Boyd, "Simple, compact, high-performance permanent-magnet faraday isolator," Opt. Lett. **11**(10), 623–625 (1986).
15. H. Dötsch, N. Bahlmann, O. Zhuromskyy, *et al.*, "Applications of magneto-optical waveguides in integrated optics: review," JOSA B **22**(1), 240–253 (2005).
16. L. Bi, J. Hu, P. Jiang, *et al.*, "On-chip optical isolation in monolithically integrated non-reciprocal optical resonators," Nat. Photonics **5**(12), 758–762 (2011).
17. L. Fan, J. Wang, L. T. Varghese, *et al.*, "An all-silicon passive optical diode," Science **335**(6067), 447–450 (2012).
18. B. Peng, Ş. K. Özdemir, F. Lei, *et al.*, "Parity-time-symmetric whispering-gallery microcavities," Nat. Phys. **10**(5), 394–398 (2014).
19. L. Chang, X. Jiang, S. Hua, *et al.*, "Parity-time symmetry and variable optical isolation in active-passive-coupled microresonators," Nat. Photonics **8**(7), 524–529 (2014).
20. Y. Yu, Y. Chen, H. Hu, *et al.*, "Nonreciprocal transmission in a nonlinear photonic-crystal fano structure with broken symmetry," Laser Photonics Rev. **9**(2), 241–247 (2015).
21. L. Del Bino, J. M. Silver, M. T. M. Woodley, *et al.*, "Microresonator isolators and circulators based on the intrinsic nonreciprocity of the kerr effect," Optica **5**(3), 279 (2018).
22. D. L. Sounas and A. Alù, "Fundamental bounds on the operation of fano nonlinear isolators," Phys. Rev. B **97**(11), 115431 (2018).
23. D. L. Sounas, J. Soric, and A. Alù, "Broadband passive isolators based on coupled nonlinear resonances," Nat. Electron. **1**(2), 113–119 (2018).
24. P. Yang, X. Xia, H. He, *et al.*, "Realization of nonlinear optical nonreciprocity on a few-photon level based on atoms strongly coupled to an asymmetric cavity," Phys. Rev. Lett. **123**(23), 233604 (2019).
25. L. Tang, J. Tang, H. Wu, *et al.*, "Broad-intensity-range optical nonreciprocity based on feedback-induced kerr nonlinearity," Photonics Res. **9**(7), 1218–1225 (2021).
26. R.-K. Pan, L. Tang, K. Xia, *et al.*, "Dynamic nonreciprocity with a kerr nonlinear resonator," Chin. Phys. Lett. **39**(12), 124201 (2022).
27. L. Tang, J. Tang, M. Chen, *et al.*, "Quantum squeezing induced optical nonreciprocity," Phys. Rev. Lett. **128**(8), 083604 (2022).
28. A. D. White, G. H. Ahn, K. V. Gasse, *et al.*, "Integrated passive nonlinear optical isolators," Nat. Photonics **17**(2), 143–149 (2023).
29. R.-K. Pan, L. Tang, and K. Xia, "Broadband dynamic nonreciprocity based on a nonlinear mach-zehnder interferometer," Phys. Rev. A **110**(4), 043505 (2024).
30. H. Lira, Z. Yu, S. Fan, *et al.*, "Electrically driven nonreciprocity induced by interband photonic transition on a silicon chip," Phys. Rev. Lett. **109**(3), 033901 (2012).
31. Z. Yu and S. Fan, "Complete optical isolation created by indirect interband photonic transitions," Nat. Photonics **3**(2), 91–94 (2009).
32. N. A. Estep, D. L. Sounas, J. Soric, *et al.*, "Magnetic-free non-reciprocity and isolation based on parametrically modulated coupled-resonator loops," Nat. Phys. **10**(12), 923–927 (2014).
33. D. L. Sounas and A. Alù, "Non-reciprocal photonics based on time modulation," Nat. Photonics **11**(12), 774–783 (2017).
34. C. W. Peterson, W. A. Benalcazar, M. Lin, *et al.*, "Strong nonreciprocity in modulated resonator chains through synthetic electric and magnetic fields," Phys. Rev. Lett. **123**(6), 063901 (2019).
35. A. Pandey, S. Dwivedi, T. Zhenzhou, *et al.*, "Nonreciprocal light propagation in a cascaded all-silicon microring modulator," ACS Photonics **8**(7), 1997–2006 (2021).
36. A. Zarif and K. Jamshidi, "Non-reciprocity in a silicon photonic ring resonator with time-modulated regions," Opt. Express **32**(15), 26938–26953 (2024).
37. K. Xia, G. Lu, G. Lin, *et al.*, "Reversible nonmagnetic single-photon isolation using unbalanced quantum coupling," Phys. Rev. A **90**(4), 043802 (2014).
38. C. Sayrin, C. Junge, R. Mitsch, *et al.*, "Nanophotonic optical isolator controlled by the internal state of cold atoms," Phys. Rev. X **5**(4), 041036 (2015).
39. M. Scheucher, A. Hilico, E. Will, *et al.*, "Quantum optical circulator controlled by a single chirally coupled atom," Science **354**(6319), 1577–1580 (2016).
40. L. Tang, J. Tang, W. Zhang, *et al.*, "On-chip chiral single-photon interface: Isolation and unidirectional emission," Phys. Rev. A **99**(4), 043833 (2019).
41. S. Guddala, Y. Kawaguchi, F. Komissarenko, *et al.*, "All-optical nonreciprocity due to valley polarization pumping in transition metal dichalcogenides," Nat. Commun. **12**(1), 3746 (2021).
42. J.-S. Tang, W. Nie, L. Tang, *et al.*, "Nonreciprocal single-photon band structure," Phys. Rev. Lett. **128**(20), 203602 (2022).

43. S. Manipatruni, J. T. Robinson, and M. Lipson, "Optical nonreciprocity in optomechanical structures," Phys. Rev. Lett. **102**(21), 213903 (2009).
44. X.-W. Xu and Y. Li, "Optical nonreciprocity and optomechanical circulator in three-mode optomechanical systems," Phys. Rev. A **91**(5), 053854 (2015).
45. Z. Shen, Y.-L. Zhang, Y. Chen, *et al.*, "Experimental realization of optomechanically induced non-reciprocity," Nat. Photonics **10**(10), 657–661 (2016).
46. X. Xu, Y. Zhao, H. Wang, *et al.*, "Quantum nonreciprocality in quadratic optomechanics," Photonics Res. **8**(2), 143 (2020).
47. S.-T. Huang, Y.-B. Qian, Z.-Y. Zhang, *et al.*, "Nonreciprocal photon transport in a chiral optomechanical system," Adv. Quantum Technol. **7**(11), 2400217 (2024).
48. K. O. Hill, Y. Fujii, D. C. Johnson, *et al.*, "Photosensitivity in optical fiber waveguides: Application to reflection filter fabrication," Appl. Phys. Lett. **32**(10), 647–649 (1978).
49. B. S. Kawasaki, K. O. Hill, D. C. Johnson, *et al.*, "Narrow-band bragg reflectors in optical fibers," Opt. Lett. **3**(2), 66–68 (1978).
50. K. Hill and G. Meltz, "Fiber bragg grating technology fundamentals and overview," J. Lightwave Technol. **15**(8), 1263–1276 (1997).
51. A. Othonos, "Fiber bragg gratings," Rev. Sci. Instrum. **68**(12), 4309–4341 (1997).
52. J. Albert, L.-Y. Shao, and C. Caucheteur, "Tilted fiber bragg grating sensors," Laser Photonics Rev. **7**(1), 83–108 (2013).
53. J. Geng, S. Staines, Z. Wang, *et al.*, "Highly stable low-noise brillouin fiber laser with ultranarrow spectral linewidth," IEEE Photonics Technol. Lett. **18**(17), 1813–1815 (2006).
54. W. Loh, J. Stuart, D. Reens, *et al.*, "Operation of an optical atomic clock with a brillouin laser subsystem," Nature **588**(7837), 244–249 (2020).
55. W. Zhang and J. Yao, "A fully reconfigurable waveguide bragg grating for programmable photonic signal processing," Nat. Commun. **9**(1), 1396 (2018).
56. M. Kulishov, J. M. Laniel, N. Bélanger, *et al.*, "Nonreciprocal waveguide bragg gratings," Opt. Express **13**(8), 3068–3078 (2005).
57. M. Fujii, A. Maitra, C. Poulton, *et al.*, "Non-reciprocal transmission and schmitt trigger operation in strongly modulated asymmetric wbgs," Opt. Express **14**(26), 12782–12793 (2006).
58. S. A. R. Horsley, J.-H. Wu, M. Artoni, *et al.*, "Optical nonreciprocity of cold atom bragg mirrors in motion," Phys. Rev. Lett. **110**(22), 223602 (2013).
59. D.-W. Wang, H.-T. Zhou, M.-J. Guo, *et al.*, "Optical Diode Made from a Moving Photonic Crystal," Phys. Rev. Lett. **110**(9), 093901 (2013).
60. H. Ramezani, P. K. Jha, Y. Wang, *et al.*, "Nonreciprocal localization of photons," Phys. Rev. Lett. **120**(4), 043901 (2018).
61. Z. Lin, H. Ramezani, T. Eichelkraut, *et al.*, "Unidirectional invisibility induced by $\mathcal{PT}$-symmetric periodic structures," Phys. Rev. Lett. **106**(21), 213901 (2011).
62. M. L. Clifford R. Pollock, *Integrated Photonics* (Springer, US, 2003), 1st ed. Chap. 6.
63. Z. Ye, P. Zhao, K. Twayana, *et al.*, "Overcoming the quantum limit of optical amplification in monolithic waveguides," Sci. Adv. **7**(38), eabi8150 (2021).
64. M. Gao, Q.-F. Yang, Q.-X. Ji, *et al.*, "Probing material absorption and optical nonlinearity of integrated photonic materials," Nat. Commun. **13**(1), 3323 (2022).
65. R. W. Boyd, *Nonlinear Optics* (Elsevier, 2008), 3rd ed. Chap. 4.
66. J. Liu, G. Huang, R. N. Wang, *et al.*, "High-yield, wafer-scale fabrication of ultralow-loss, dispersion-engineered silicon nitride photonic circuits," Nat. Commun. **12**(1), 2236 (2021).
67. M. S. Kang, A. Butsch, and P. S. J. Russell, "Reconfigurable light-driven opto-acoustic isolators in photonic crystal fibre," Nat. Photonics **5**(9), 549–553 (2011).
68. D. A. Fuhrmann, S. M. Thon, H. Kim, *et al.*, "Dynamic modulation of photonic crystal nanocavities using gigahertz acoustic phonons," Nat. Photonics **5**(10), 605–609 (2011).
69. D. B. Sohn, S. Kim, and G. Bahl, "Time-reversal symmetry breaking with acoustic pumping of nanophotonic circuits," Nat. Photonics **12**(2), 91–97 (2018).
70. G. Calajó, M. J. A. Schuetz, H. Pichler, *et al.*, "Quantum acousto-optic control of light-matter interactions in nanophotonic networks," Phys. Rev. A **99**(5), 053852 (2019).
71. F. Yang, F. Gyger, and L. Thévenaz, "Intense brillouin amplification in gas using hollow-core waveguides," Nat. Photonics **14**(11), 700–708 (2020).